Channel-parameter estimation for satellite-to-submarine continuous-variable quantum key distribution

Ying Guo,[1] Cailang Xie,[1] Peng Huang,[2] Jiawei Li,[1] Ling Zhang,[1,*] Duan Huang,[1] and Guihua Zeng[2]
[1]*School of Information Science and Engineering, Central South University, Changsha 410083, China*
[2]*State Key Laboratory of Advanced Optical Communication Systems and Networks, and Center of Quantum Information Sensing and Processing, Shanghai Jiao Tong University, Shanghai 200240, China*

(Received 25 January 2018; published 24 May 2018)

This paper deals with a channel-parameter estimation for continuous-variable quantum key distribution (CV-QKD) over a satellite-to-submarine link. In particular, we focus on the channel transmittances and the excess noise which are affected by atmospheric turbulence, surface roughness, zenith angle of the satellite, wind speed, submarine depth, etc. The estimation method is based on proposed algorithms and is applied to low-Earth orbits using the Monte Carlo approach. For light at 550 nm with a repetition frequency of 1 MHz, the effects of the estimated parameters on the performance of the CV-QKD system are assessed by a simulation by comparing the secret key bit rate in the daytime and at night. Our results show the feasibility of satellite-to-submarine CV-QKD, providing an unconditionally secure approach to achieve global networks for underwater communications.

DOI: 10.1103/PhysRevA.97.052326

I. INTRODUCTION

Underwater communication is of crucial importance for undersea exploitation and modern communication. Drawbacks exist in the traditional ways of applying the underwater acoustic technique, including a low bandwidth, a large propagation delay, and security issues. Nowadays, underwater optical communication with a high bandwidth and low latency has motivated worldwide interest and has gradually become a widely used method in the new era of marine economy. Several studies have been done to improve the data bandwidth and bit error rate of underwater optical communication [1–3]. With respect to security, although underwater optical communication is naturally regarded as a more secure approach compared with underwater acoustic communication, some security vulnerabilities still exist [4]. Fortunately, the feasibility of quantum communication over seawater has been investigated theoretically [5] and has been demonstrated experimentally [6], which has provided a reliable method to achieve the goal of unconditional communication security for underwater optical communication. Due to underwater absorption and scattering, the distance of underwater optical communication would hardly be long enough for practical purposes. For instance, in seawater farther from the coastline, whose loss to photons in the blue-green window can be as low as 0.018 m^{-1} [7,8], an achievable distance of quantum communication was derived as 885 m [6].

Although the achievable distance of underwater quantum communication is shorter compared to fiber and air channels, it still can be applied to some special applications. For example, an encrypted message can be sent from an airborne platform to a submerged platform, even it is close to the surface [9]. Particularly, by using satellite quantum key distribution (QKD) technologies, it is possible to share encrypted keys between satellites and submarines, or two submarine vehicles through the same satellite. This potentially allows one to establish a global-scale underwater communication network, which means getting rid of the constraints of short communication distances.

Currently, two available approaches, referred to as discrete-variable QKD [10–13] and continuous-variable (CV) QKD [14–17], are employed to distribute secret keys in free-space and satellite-to-ground quantum communications. For a general CV-QKD system, Alice usually encodes the information in quadratures of a light field with Gaussian modulation. At Bob's side, the weak signal light is measured by interfering with a strong local oscillator (LO) in a shot-noise-limited homodyne detector [18–20]. It is noteworthy that the LO plays the role of a spatial and spectral filter, which allows unrestrained daylight operation during the CV-QKD run [21]. Beyond that, the CV-QKD has practical potential advantages as it is compatible with standard optical communication technologies. Therefore, applying the CV-QKD approach to the satellite-to-submarine scenario has a practical significance for achieving secure global underwater communication networks.

The purpose of this paper is to derive a satellite-to-submarine channel model for CV-QKD. Based on the proposed algorithms, the channel parameters, including transmittances and excess noise, are estimated using the Monte Carlo simulation. Compared with a linear channel such as fiber, the transmittance of the free-space channel is unstable and fluctuates randomly in time due to atmospheric turbulence [22–24]. Besides that, the roughness of the sea surface should also be considered to be a factor that results in fluctuating transmittance [25,26]. On the other hand, background light is regarded as the main noise and is discussed in both daytime and night scenarios. Then, we compare the performance of the CV-QKD system over a satellite-to-submarine link at

*Corresponding author: lingzhang2017@foxmail.com

different low-Earth orbits in both the daytime and at night. The results show that under various interference factors, such as the zenith angle of the satellite, wind speed, and submarine depth, secret keys could be successfully established against collective attacks even in the daytime.

This paper is organized as follows: In Sec. II, we first introduce the strategy of the CV-QKD over satellite-to-submarine links. The transmittance distributions of the fluctuating quantum channels are estimated using the Monte Carlo method. In Sec. III, we analyze the noise characteristics, including initial excess noise and background light noise. In Sec. IV, we give a performance analysis of the CV-QKD with a finite-size effect over a satellite-to-submarine link, and, finally, a conclusion is drawn in Sec. V.

II. TRANSMITTANCE ANALYSIS

Figure 1(a) illustrates the schematic of the CV-QKD system over a satellite-to-submarine link. On the satellite (i.e., Alice) side, the information is modulated on Gaussian states using electro-optical modulators. The quantum states have to pass through two transmission media before arriving at the submarine vehicle, that is, a turbulent atmosphere and high-loss seawater. The roughness of the sea surface also plays an important role in affecting the transmitted light. At the submarine vehicle (i.e., Bob) site, the phase front distortions of the received light are corrected by an adaptive optics system. Then, the quantum light is detected using a coherent measurement with the LO, which is generated by a local laser [27–29]. In order to keep the attenuation of the satellite-to-submarine link as small as possible, we make a compromise between the transmission window of the atmosphere and the blue-green window of seawater, which are around 800 [30] and 400–500 nm [31], respectively. Figure 1(b) shows a comparison of the atmospheric transmittance and the attenuation of clear ocean water, which are both affected by absorption and scattering. The numerical simulation of the atmospheric transmittance comes from the software package MODTRAN, for a navy aerosol model at an altitude of 20 km from the sea surface. The attenuation coefficient of seawater $c(\lambda)$ is defined as the sum of the absorption coefficient $a(\lambda)$ and scattering coefficient $b(\lambda)$ [4,32]. The expressions are as follows,

$$a(\lambda) = [a_w(\lambda) + 0.06a_c(\lambda)C^{0.65}][1 + 0.2e^{-0.014(\lambda-440)}],$$
$$b(\lambda) = 0.3\frac{550}{\lambda}C^{0.62}, \quad c(\lambda) = a(\lambda) + b(\lambda), \tag{1}$$

where λ is the wavelength, C is the chlorophyll concentration, $a_w(\lambda)$ is the absorption coefficient in ocean water, and $a_c(\lambda)$ is the statistically derived chlorophyll-specific absorption coefficient. Comparing atmospheric transmittance with underwater attenuation, we choose a reasonable laser wavelength at around 550 nm for propagating through the satellite-to-submarine channel.

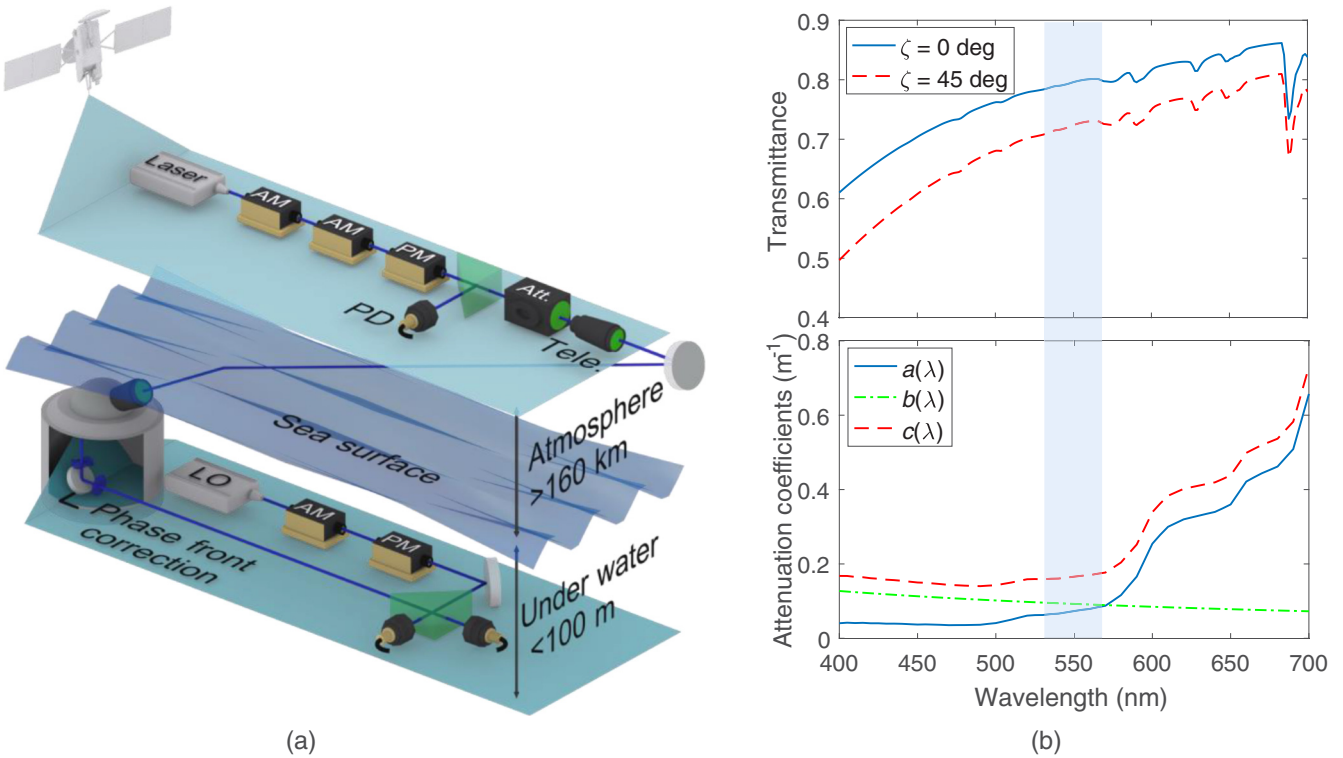

FIG. 1. (a) The scheme of CV-QKD over a satellite-to-submarine link. Modulated light is transmitted through the atmosphere, sea surface, and seawater, in that order. With the LO, which is generated by a local laser, Bob (submarine vehicle) measures the states using homodyne detection. (b) The top and bottom figures represent the atmospheric transmittance and clear ocean water attenuation as functions of wavelength, respectively, which are both incurred by absorption and scattering. AM: amplitude modulator; PM: phase modulator; PD: photodiode; Tele.: telescope; Att.: attenuator; LO: local oscillator; ζ: zenith angle of the satellite.

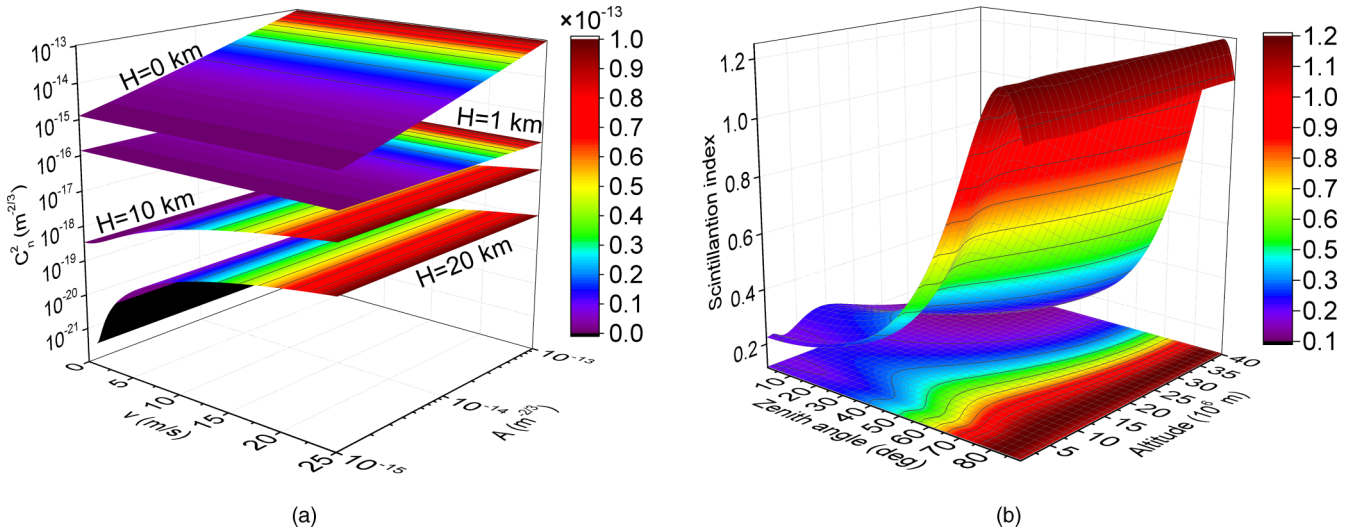

(a) (b)

FIG. 2. (a) The refraction structure C_n^2 at altitudes of 0, 1, 10, and 20 km with various wind speeds and constant parameter A. (b) The scintillation index as a function of the zenith angle of a satellite at altitudes from 200 to 40 000 km.

A. Atmospheric turbulence effect

The main factor limiting the performance of free-space optical communication is atmospheric turbulence, which could result in beam wandering and beam broadening. In particular, turbulent eddies whose size is large compared to the size of the beam induce beam wandering, while smaller-scale turbulent features induce beam broadening [33]. As a result, the received irradiance of the optical wave fluctuates in time, which can be characterized by the scintillation index. In fact, several scintillation models for optical beam propagation over a satellite-to-ground link have been investigated in the literature [34–36]. With the existence of large zenith angles, the scintillation index model for a satellite-to-submarine link could be given by

$$\delta_I^2 = \exp\left[\frac{0.49\delta_R^2}{\left(1+1.11\delta_R^{12/5}\right)^{7/6}} + \frac{0.51\delta_R^2}{\left(1+0.69\delta_R^{12/5}\right)^{5/6}}\right] - 1, \quad (2)$$

the Rytov variance δ_R^2 is defined as

$$\delta_R^2 = 2.25k^{7/6}\sec^{11/6}(\zeta)\int_{h_0}^{H} C_n^2(h)(h-h_0)^{5/6}dh, \quad (3)$$

where $k = 2\pi/\lambda$ is the optical wave number, $H = h_0 + L\cos\zeta$ is the satellite altitude ($h_0 = 0$ in the satellite-to-submarine link), L is the propagation distance, ζ is the zenith angle, and $C_n^2(h)$ is the refraction index structure constant parameter. One of the most widely used $C_n^2(h)$ is the Hufnagel-Valley (HV) model described by [37]

$$C_n^2(h) = 0.00594(v/27)^2(h\times 10^{-5})^{10}e^{-\frac{h}{1000}} + 2.7\times 10^{-16}e^{-\frac{h}{1500}} + Ae^{-\frac{h}{100}}, \quad (4)$$

where v is the pseudowind in meters per second (m/s) and A is the nominal value of $C_n^2(0)$ in $\mathrm{m}^{-2/3}$. Figure 2(a) illustrates C_n^2 in satellite altitudes of 0, 1, 10, and 20 km based on varying wind speed and constant $C_n^2(0)$. In the satellite-to-submarine scenario, $C_n^2(0)$ expresses the atmospheric refraction structure above the ocean near-surface. From the weather research and forecasting (WRF) model outputs [38], the near-surface refractive index structure constant mainly varies in the range of 10^{-15}–10^{-13} $\mathrm{m}^{-2/3}$. The wind speed v can be extracted from the European Centre for Medium-Range Weather Forecasts (ECMWF) Re-Analysis (ERA-Interim) data set [39], which ranges roughly from 0 to 26 m/s. We can see clearly that the ocean near-surface turbulence level has little effect above 1 km and wind speed governs the profile behavior primarily in the vicinity of 10 km. Besides, atmospheric turbulence could be negligible when the altitude is higher than 10 km.

In order to calculate the scintillation index, we take the mean value of $C_n^2(0)$ which is estimated using the WRF model [38], i.e., $C_n^2(0) = 9.6\times 10^{-14}$ $\mathrm{m}^{-2/3}$, and take the prevailing wind speed 6 m/s in the ERA-Interim data set. As shown in Fig. 2(b), the main determinant of the scintillation index is the zenith angle when the satellite is higher than 10 km. Considering both the Earth's radius and the satellite altitude, the maximal zenith angle at certain altitudes can be calculated by $\zeta_{\max} = \arcsin[R_{\mathrm{earth}}/(R_{\mathrm{earth}}+H)]$, where R_{earth} is the Earth's radius. The maximum could be up to around 76° when $H = 200$ km. Therefore, in a practical satellite-to-submarine CV-QKD system, the zenith angle $\zeta > 60°$ should also be taken into account.

As a quantum channel, the atmosphere should be characterized by fluctuating transmission properties. Also, the Gaussian quantum state degrades to a non-Gaussian mixed state after transmitting through a fluctuating channel whose transmittance could be estimated by a probability distribution. At present, based on the elliptic beam approximation, the probability distribution for atmospheric transmittance can be derived from the Glauber-Sudarshan P function [24,40], which yields a better agreement with the experimental data [23] than the log-normal model [41]. Atmospheric quantum links under diverse weather conditions have also been analyzed based on the elliptic model [42].

Combining the scintillation index and the elliptic beam model, atmospheric transmittance distribution could be derived as shown in Fig. 3(a). First of all, atmospheric turbulence causes beam wandering and broadening, both of which are

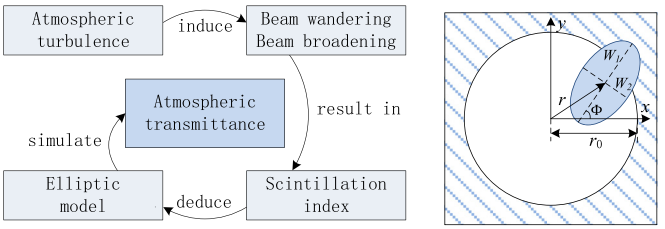

(a) (b)

FIG. 3. (a) The derivation process of atmospheric transmittance and (b) the aperture of radius r_0 and the elliptical beam profile with the half axis W_1 and W_2, where W_1 rotates on the angle Φ relating to the x axis. Beam wandering is characterized by parameter r, which represents the beam-centroid position with respect to the center of the aperture.

components contributing to the scintillation index. Then, the elliptic model in Fig. 3(b) can be deduced, which applies five parameters, (x_0, y_0, W_1, W_2) and Φ, to uniquely describe any spot on the aperture plane. Here, (x_0, y_0) is the beam-centroid position, (W_1, W_2) expresses the half axis of the elliptical beam profile, and Φ is the rotated angle of W_1 related to the x axis of the aperture. Correspondingly, the position (x_0, y_0) describes beam wandering, while (W_1, W_2) and Φ characterize beam broadening and deformation. With this elliptic assumption, the atmospheric transmittance of the satellite-to-submarine link can be approximated by

$$T_{\text{air}} = T_0 \exp\left\{-\left[\frac{r/r_0}{\mathrm{R}\left(\frac{2}{\mathrm{W}_{\text{eff}}(\phi-\varphi_0)}\right)}\right]^{\lambda\left(\frac{2}{\mathrm{W}_{\text{eff}}(\phi-\varphi_0)}\right)}\right\}, \tag{5}$$

where r_0 is the aperture radius, r is the beam deflection distance, T_0 is the maximal transmission coefficient at $r = 0$, and W_{eff} is the effective spot radius. Here, $\lambda(\xi)$ and $\mathrm{R}(\xi)$ correspond to the shape and scale functions, respectively, which are defined by

$$\begin{aligned}\lambda(\xi) &= 2r_0^2\xi^2 \frac{\exp\left(-r_0^2\xi^2\right)\mathrm{I}_1\left(r_0^2\xi^2\right)}{1-\exp\left(-r_0^2\xi^2\right)\mathrm{I}_0\left(r_0^2\xi^2\right)} \\ &\quad\times\left[\ln\left(2\frac{1-\exp\left(-\frac{1}{2}r_0^2\xi^2\right)}{1-\exp\left(-r_0^2\xi^2\right)\mathrm{I}_0\left(r_0^2\xi^2\right)}\right)\right], \\ \mathrm{R}(\xi) &= \left[\ln\left(2\frac{1-\exp\left(-\frac{1}{2}r_0^2\xi^2\right)}{1-\exp\left(-r_0^2\xi^2\right)\mathrm{I}_0\left(r_0^2\xi^2\right)}\right)\right]^{-\frac{1}{\lambda(\xi)}},\end{aligned} \tag{6}$$

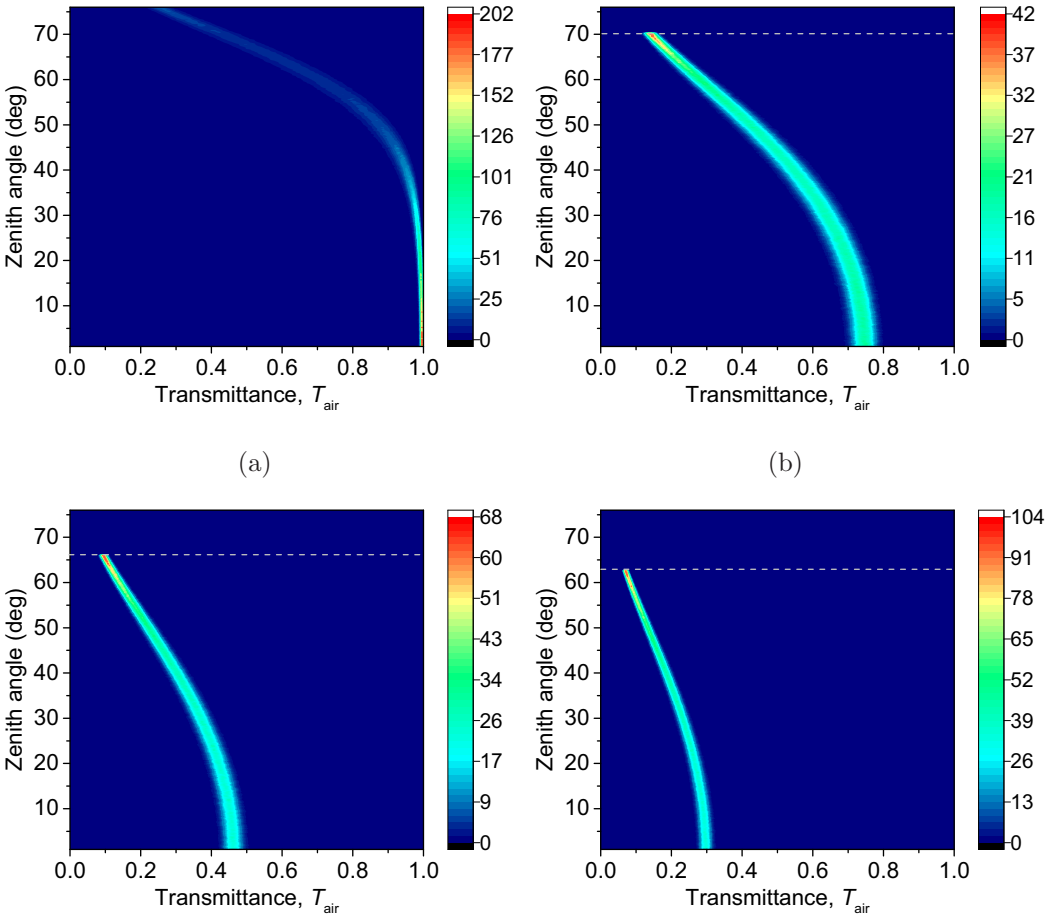

FIG. 4. The probability density distribution of atmospheric transmittance with various zenith angles. The low-Earth orbits of the satellite are set to (a) 200, (b) 400, (c) 600, and (d) 800 km. The dashed lines represent the maximal zenith angle at the corresponding altitudes.

where $\mathrm{I_n}$ are the modified Bessel functions. The transmittance T_0 can be estimated by

$$T_0 = 1 - \mathrm{I}_0\left(r_0^2\frac{W_1^2 - W_2^2}{W_1^2W_2^2}\right)\exp\left[-r_0^2\frac{W_1^2 + W_2^2}{W_1^2W_2^2}\right] - 2\left\{1 - \exp\left[-\frac{r_0^2}{2}\left(\frac{1}{W_1} - \frac{1}{W_2}\right)^2\right]\right\} \times \exp\left\{-\left[\frac{\frac{(W_1+W_2)^2}{|W_1^2-W_2^2|}}{\mathrm{R}\left(\frac{1}{W_1} - \frac{1}{W_2}\right)}\right]^{\lambda\left(\frac{1}{W_1} - \frac{1}{W_2}\right)}\right\}. \tag{7}$$

For the given angle $\theta = \Phi - \varphi_0$, the effective spot radius $\mathrm{W_{eff}}(\theta)$ can be approximated as

$$\mathrm{W}_{\mathrm{eff}}^2(\theta) = 4r_0^2\left\{\mathcal{W}\left(\frac{4r_0^2}{W_1W_2}\exp\left[\frac{r_0^2}{W_1^2}(1 + 2\cos^2\theta)\right] \times \exp\left[\frac{r_0^2}{W_2^2}(1 + 2\sin^2\theta)\right]\right)\right\}^{-1}, \tag{8}$$

where $\mathcal{W}(x)$ is the Lambert function.

Based on Eqs. (5)–(8), the probability distribution of atmospheric transmittance can be evaluated using the Monte Carlo method. As the turbulence of the atmosphere above the ocean can be regard as isotropic [43], the distributions of the parameters (x_0, y_0, W_1, W_2) and ϕ could be derived from the Gaussian approximation [24]. First, ϕ is uniformly distributed and independent of (x_0, y_0, W_1, W_2). Second, the beam-centroid position (x_0, y_0) follows a Gaussian distribution as it can be considered to be affected by additive white Gaussian noise. Third, the shape parameters (W_1, W_2) can be obtained by multiplying a large number of small random contributions, which gives a good argument for assuming that (W_1, W_2) is log-normally distributed. For a given $\Theta_i = \ln\frac{W_i^2}{W_0}$, $i = 1,2$, where W_0 is the transmitter beam radius, the correlation of $(x_0, y_0, \Theta_1, \Theta_2)$ could be defined by its covariance matrix [24,42], which reads

$$\mathcal{M} = \begin{pmatrix} \langle x_0^2\rangle & 0 & 0 & 0 \\ 0 & \langle y_0^2\rangle & 0 & 0 \\ 0 & 0 & \langle\Theta_1^2\rangle & \langle\Theta_1\Theta_2\rangle \\ 0 & 0 & \langle\Theta_1\Theta_2\rangle & \langle\Theta_2^2\rangle \end{pmatrix}. \tag{9}$$

Combining the results of the scintillation index in Eq. (4) with the turbulent regimes in Ref. [24] ($\delta_I^2 < 1$, $\delta_I^2 \approx 1 \ldots 10$, and $\delta_I^2 \gg 1$ correspond to weak, moderate, and strong turbulence, respectively), the satellite-to-submarine link could be regarded as affected by weak-to-moderate turbulence. Therefore, the elements of $\mathcal{M}$ can be expressed by

$$\langle x_0^2\rangle = \langle y_0^2\rangle = 0.33W_0^2\delta_I^2\Omega^{-7/6},$$
$$\langle\Theta_1^2\rangle = \langle\Theta_2^2\rangle = \ln\left[1 + \frac{1.2\delta_I^2\Omega^{5/6}}{\left(1 + 2.96\delta_I^2\Omega^{5/6}\right)^2}\right],$$
$$\langle\Theta_1\Theta_2\rangle = \ln\left[1 - \frac{0.8\delta_I^2\Omega^{5/6}}{\left(1 + 2.96\delta_I^2\Omega^{5/6}\right)^2}\right], \tag{10}$$

where $\Omega = \frac{kW_0^2}{2L}$ is the Fresnel parameter of the beam. Their expectations read

$$\langle x_0\rangle = \langle y_0\rangle = 0,$$
$$\langle\Theta_1\rangle = \langle\Theta_2\rangle = \ln\left[\frac{\left(1 + 2.96\delta_I^2\Omega^{5/6}\right)^2}{\Omega^2\sqrt{\left(1 + 2.96\delta_I^2\Omega^{5/6}\right)^2 + 1.2\delta_I^2\Omega^{5/6}}}\right]. \tag{11}$$

Based on the above parameter approximation, Fig. 4 shows the density distributions of atmospheric transmittance using the Monte Carlo simulation. The dashed lines represent the maximal zenith angles at the corresponding altitudes. The effects of zenith angle on atmospheric transmittance T_{air} are simulated at four different low-Earth orbits, i.e., 200, 400, 600, and 800 km. It is obvious that for each certain altitude, the fluctuating transmittance tends to decrease and distribute in a smaller area with increasing zenith angle. When the altitude increases, the atmospheric transmittance distributes at a lower range with the corresponding zenith angle. The parameters W_0 and r_0 are assigned to be 6 cm and 1 m, respectively.

B. Sea surface effect

The sea surface plays an important role in the satellite-to-submarine scenario, which causes propagating light deflection and refraction. It affects the total link efficiency together with atmospheric turbulence and optical underwater loss, as we will show in the security analysis. In this section, we will focus on investigating the influence of a rough sea surface when light is incoming from a different zenith angle. So far, several techniques have been presented for describing the variations of the surface. A general model that has been presented by Cox and Munk (CM) [25], which described a method developed for interpreting the statistics of the Sun's glitter on the sea

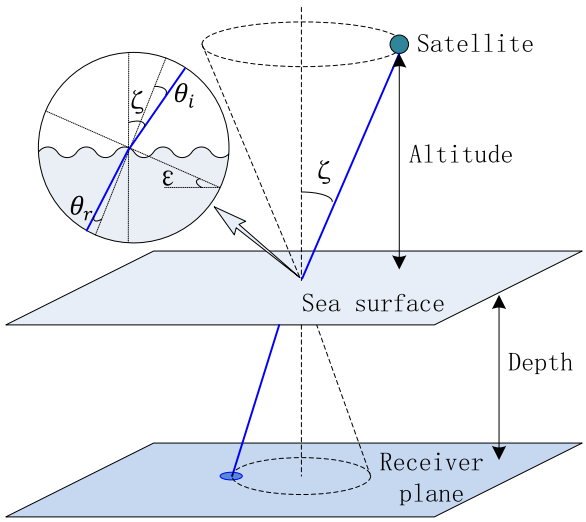

FIG. 5. The geometric model of the satellite, sea surface, and receiver plane. The top dotted circle contains the possible positions of the satellite at certain altitudes and zenith angle ζ. In the magnification of the local sea surface, ε corresponds to the wave slope while θ_i and θ_r represent the light incident angle and refraction angle, respectively.

surface in terms of the statistics of the slope distribution, is the widely used wind-induced wave model. They observed that the probability distribution of the crosswind slope components is nearly Gaussian, but, however, the upwind slope components need to be approximated with some extra higher moments. Consequently, the statistical characteristic of the sea surface slopes can be represented by the Gram-Charlier distribution,

$$p(Z_u,Z_c)=\frac{1}{2\pi\sigma_u\sigma_c}\exp\left[-\frac{1}{2}\left(Z_u^2+Z_c^2\right)\right]\times\left[1-\frac{1}{2}c_{21}Z_c\left(Z_u^2-1\right)-\frac{1}{6}c_{03}\left(Z_c^3-3Z_c\right)+\frac{1}{24}c_{40}\left(Z_u^4-6Z_u^2+3\right)+\frac{1}{4}c_{22}\left(Z_u^2-1\right)\left(Z_c^2-1\right)+\frac{1}{24}c_{04}\left(Z_c^4-6Z_c^2+3\right)\right], \tag{12}$$

and

$$Z_u=\frac{\varepsilon_u}{\sigma_u},\quad Z_c=\frac{\varepsilon_c}{\sigma_c}, \tag{13}$$

where ε_u and ε_c correspond to the upwind and crosswind of wave surface slopes with variances σ_u^2 and σ_c^2, respectively. The above parameters can be estimated as

$$\sigma_c^2=0.003+1.92\times10^{-3}v,\quad \sigma_u^2=3.16\times10^{-3}v$$
$$c_{21}=0.01-0.0086v,\quad c_{03}=0.04-0.033v,$$
$$c_{40}=0.4,\quad c_{22}=0.12,\quad c_{04}=0.23, \tag{14}$$

where v is the wind speed.

The CM model accords well with practical situations and is still widely used [44,45]. Based on the CM model, we will follow mainly the geometrical considerations of the sea surface in Fig. 5 which could be applied to investigate the effects on the deflection and refraction of light propagation [46]. Based on certain altitudes and zenith angles, the possible positions of the satellite compose a circular trajectory. Therefore, the received photons may also distribute around a circle, which will be seen in the following analysis. According to the process of light passing through the sea surface, the change in the light propagation direction is determined by the angle of incidence

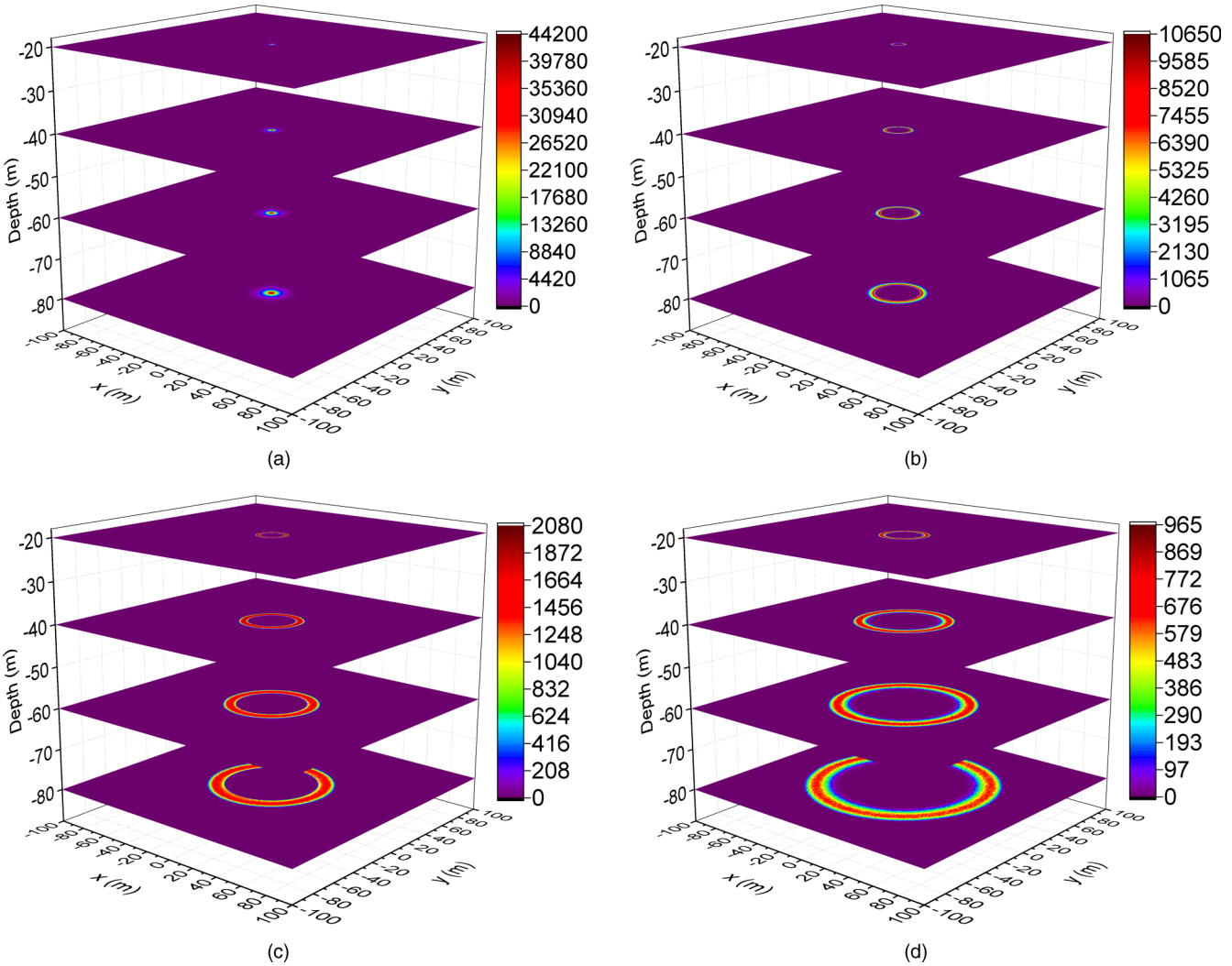

FIG. 6. The light intensity distribution derived from a rough sea surface at different depths of water. The zenith angles of the satellite are set to (a) 0°, (b) 20°, (c) 40°, and (d) 60°, respectively. The total number of photons for the Monte Carlo simulation is 10^6 for each situation and the wind speed is 3 m/s.

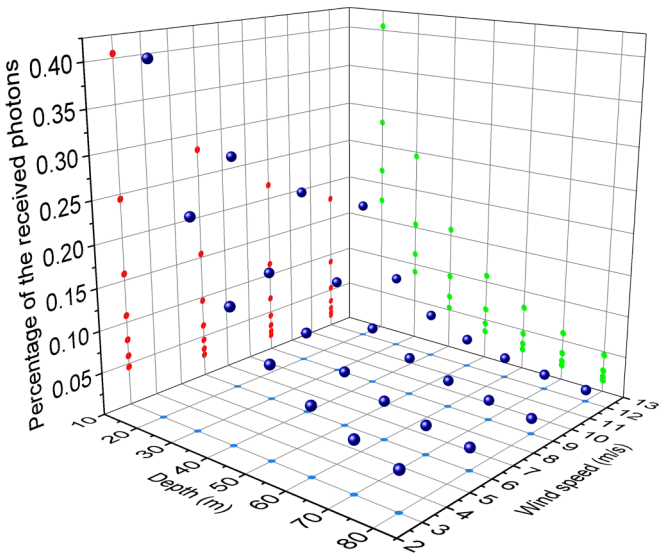

FIG. 7. The percentage of received photons as a function of different wind speeds (3, 6, 9, and 12 m/s) and depths (20, 40, 60, and 80 m). The result is based on the assumption that the zenith angle $\zeta = 0^\circ$. The number of photons used for the Monte Carlo simulation is 10^6 for each case. The radius of the receiver is 1 m.

and the refractive indices of the air and water. There are two factors affecting the angle of incidence θ_i. One is the local surface slope ε in the direction θ_s against the upwind direction, which can be derived as

$$\varepsilon = \sqrt{\varepsilon_u^2 + \varepsilon_c^2}, \quad \theta_s = \arctan\left(\frac{\varepsilon_c}{\varepsilon_u}\right), \tag{15}$$

and another is the zenith angle of the satellite. Then, the angle of refraction θ_r can be calculated by Snell's law, and expressed by $\theta_r = \arcsin\left(\frac{\sin\theta_i n_a}{n_w}\right)$, where the refractive indices of air and water, n_a and n_w, can be set to $n_a = 1.000\,293$ and $n_w = 1.34$, respectively. Figure 6 illustrates the light intensity distribution derived from the variational light propagation direction at water depths of 20, 40, 60, and 80 m. The wind speed is set to its prevailing value of 6 m/s here and the zenith angles are assigned to 0°, 20°, 40°, and 60°. With an increase in the depth of water, the beam spot gets larger at the reception plane. Compared to the results of different zenith angles, the concentrated distribution of the light intensity expands gradually in the shape of a circle with increasing zenith angle.

The light deflection which is caused by the roughness of the surface would directly affect the total link efficiency. We define $\eta_{\text{deflection}}$ to describe this part of the efficiency. In order to estimate $\eta_{\text{deflection}}$, we need to integrate the received photons

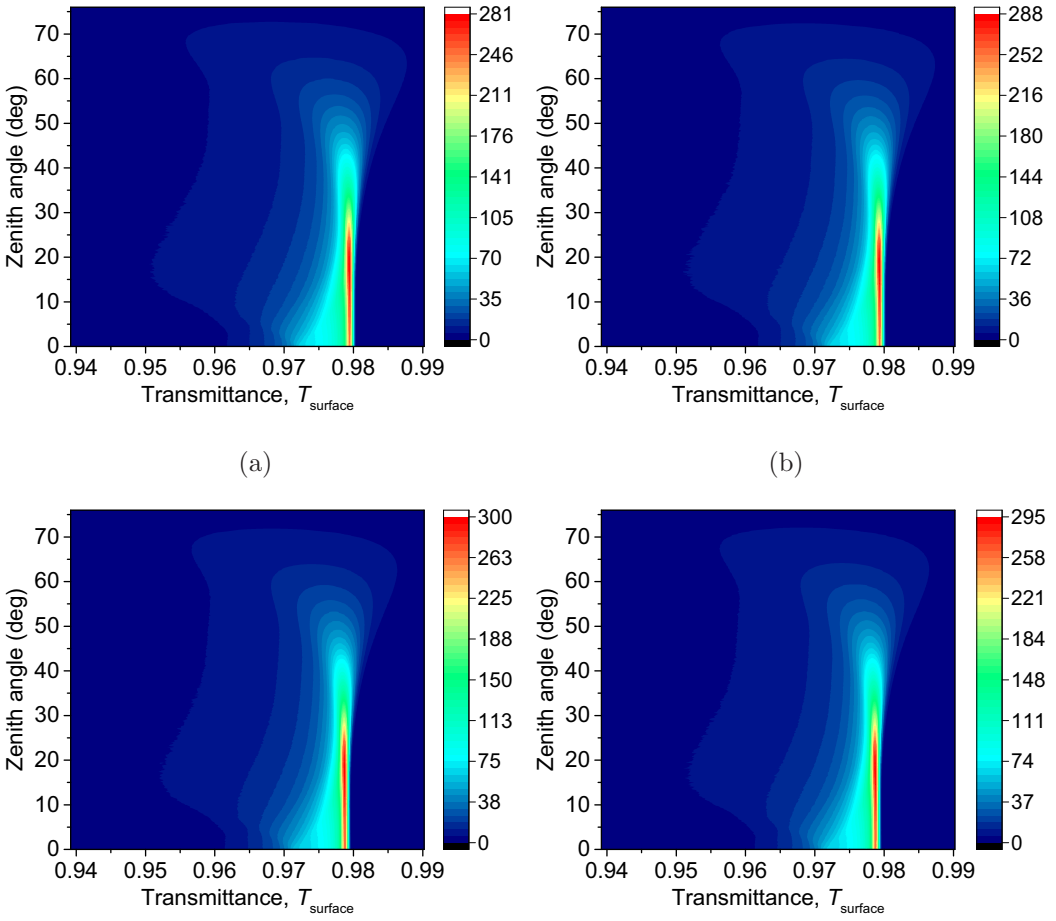

FIG. 8. The transmittance probability distribution of a rough sea surface based on different wind speeds: (a) 3, (b) 6, (c) 9, and (d) 12 m/s. The number of photons used for the Monte Carlo simulation is 10^6 for each case.

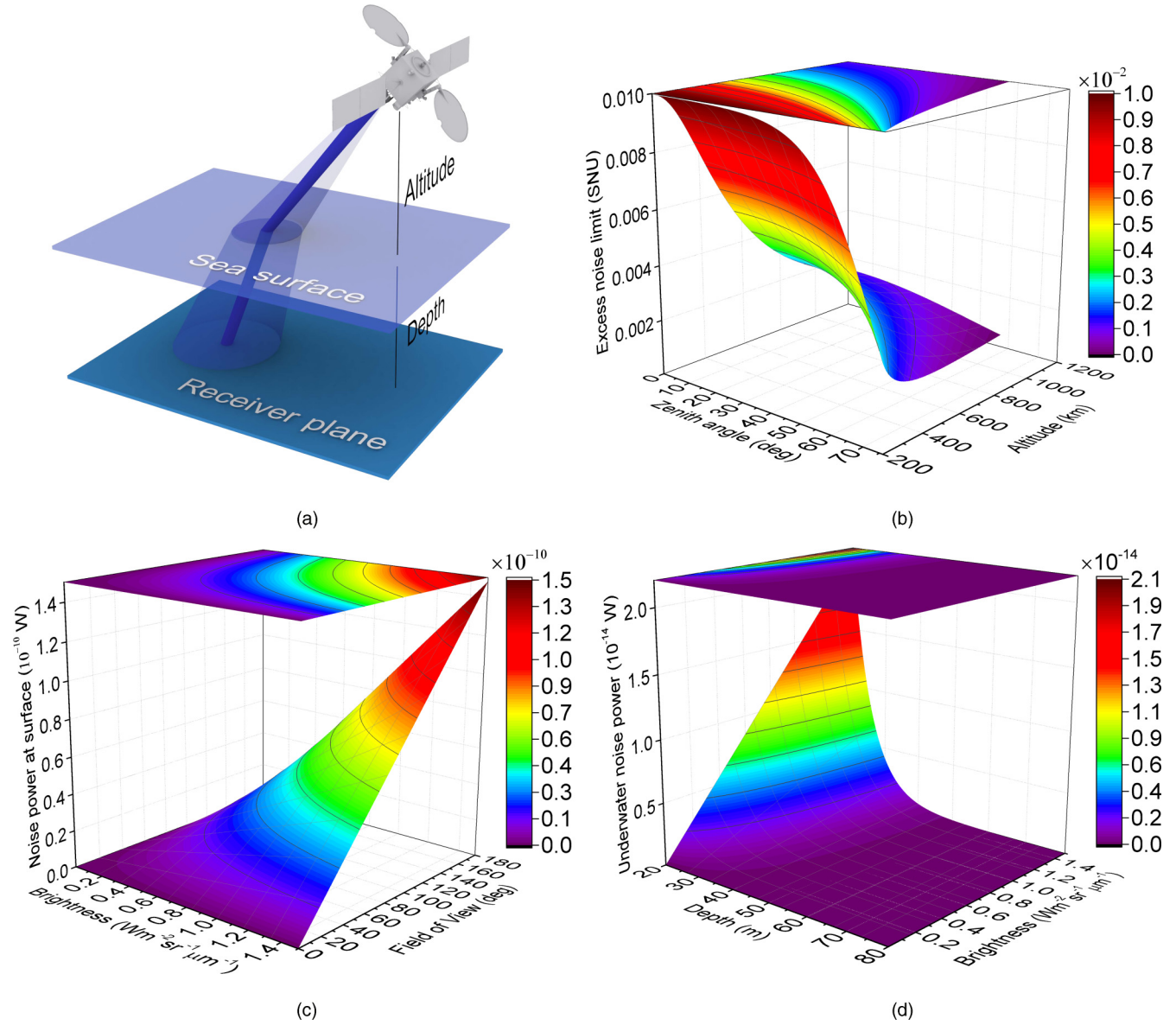

FIG. 9. (a) An ideal model of light propagation without other turbulence except intensity loss. (b) The ENL in shot-noise units (SNU). (c) The background noise power received by a virtual receiver at the surface as a function of brightness and field of view. (d) The power of background noise underwater as a function of depth and brightness. The excess noise of the initial states is 0.01 SNU. The parameters are set to $W_0 = 6$ cm, $r_0 = 1$ m, $R = 1.25\%$, $c = 0.166$ m^{-1}, and $L_{\text{fac}} = 1$.

over the receiver radius r_0 with respect to the total photons. Therefore, we assume that there are large numbers of photons through the CM-model surface and then we collect the photons that hit at the receiver aperture. With the assumption that the light direction at the satellite has been already aligned at the center of the receiver, which is equivalent to the situation where the zenith angle $\zeta = 0^\circ$, we perform Monte Carlo simulations on different wind speeds and depths. Figure 7 shows the estimated values of $\eta_{\text{deflection}}$. The total number of photons is 10^6 and the receiver radius is 1 m. It is obvious that the percentage of received photons decreases rapidly with both increasing wind speed and depth.

In order to study the effect of surface on the transmittance, the fraction of transmitted incident light can be obtained by the Fresnel formula [26]. We decompose quantum light into perpendicular and parallel components, i.e., $T_{\text{refraction},\perp}$ and $T_{\text{refraction},\parallel}$, respectively. The total Fresnel transmittance is determined by

$$T_{\text{refraction}} = \tfrac{1}{2}(T_{\text{refraction},\perp} + T_{\text{refraction},\parallel}), \tag{16}$$

and the elements are as follows,

$$T_{\text{refraction},\perp} = 1 - \frac{\sin^2(\theta_i - \theta_r)}{\sin^2(\theta_i + \theta_r)},$$
$$T_{\text{refraction},\parallel} = 1 - \frac{\tan^2(\theta_i - \theta_r)}{\tan^2(\theta_i + \theta_r)}, \tag{17}$$

where θ_i and θ_r represent the incidence angle and the refraction angle, respectively.

Figure 8 shows the probability distribution of transmittance when light passes through the sea surface. According to the geometric relationship between the Earth and the satellite, the zenith angles are set from 0° to 76° and the situations at different wind speeds are investigated. From the results it can be observed that the transmittance is distributed at around a high value of 0.979 when the zenith angle is less than 30°. With a continued increasing zenith angle, the distribution of the transmittance expands from 0.95 to 0.99. Compared to the zenith angle, wind speed has a very small impact on the transmittance distribution. Combining the efficiency of deflection, the total transmittance of the surface can be defined as $T_{\text{surface}} = \eta_{\text{deflection}} T_{\text{refraction}}$.

C. Loss in seawater

Absorption and scattering are two main factors influencing light propagation in seawater. Absorption results in the attenuation of light intensity and scattering leads to the deflection of light from its original propagation direction. Therefore, the coefficients of absorption and scattering, a and b, were introduced in Eq. (1). As light is transmitted through seawater for a short distance, we assume the underwater channel to be a linear attenuation model. Satellite-to-submarine communication occurs usually in the pelagic region, thus we restrict our discussion to attenuation at 550 nm to clear ocean water which has been simulated before. The transmittance can be calculated by $T_{\text{sea}} = 10^{-c/10}$, where c represents the total attenuation coefficient and T_{sea} has the dimension m^{-1}, and the result is around $T_{\text{sea}} = 0.9625\ \text{m}^{-1}$ (the laboratory transmittance of seawater in Ref. [47] at 550 nm is $0.933\ \text{m}^{-1}$).

III. EXCESS NOISE ANALYSIS

There are several factors which contribute to the noise in the satellite-to-submarine CV-QKD system, including lasers, modulators, background light, and detection. We first analyze the original excess noise of a general CV-QKD system over a vacuum satellite-to-submarine link and then obtain the excess noise limit (ENL). In a good approximation, the intensity distribution at the center of the Airy pattern is nearly Gaussian, which allows us to assume the vacuum quantum link to be a linear attenuation channel [16,36]. Figure 9(a) shows such an ideal scenario when light propagates from the satellite to the submarine vehicle in vacuum. The fraction of the measured power within the receiver aperture can be estimated by integration over the intensity ratio,

$$\frac{I(r,L)}{I_0} = \frac{W_0^2}{W^2} \exp\left(-\frac{2r^2}{W^2}\right), \tag{18}$$

where r and L represent the radius of the receiver and the propagation distance, respectively, $W_0 = 6$ cm is the beam waist, $W = W_0\sqrt{1 + \frac{2L}{kW_0^2}}$ is the diffractive beam radius at the receiver, and k is the wave number. The propagation distance L contains two parts, the altitude H and the depth D, and they are added by $L = H\sec(\zeta) + D\sec(\theta_r)$. In a real scenario, the fraction of depth could be negligible compared to the altitude. Integration over r in the range of $[0, r_0]$ ($r_0 = 1$ m) yields the loss in vacuum,

$$R_e = \frac{P(r_0,L)}{P_0} = 1 - \exp\left(-\frac{2r_0^2}{W^2}\right). \tag{19}$$

For practical purposes, the original excess noise ϵ_0 of the CV-QKD with Gaussian-modulated states is around 0.01 in shot-noise units (SNU) [48,49]. Scaling the initial excess noise with R_e results in the values of ENL, $\epsilon_{\text{limit}} = \epsilon_0 R_e$. As shown in Fig. 9(b), the ENL decreases with increasing zenith angle and altitude, and this is because either an increasing zenith angle or altitude, or both, could lead the propagation distance to be

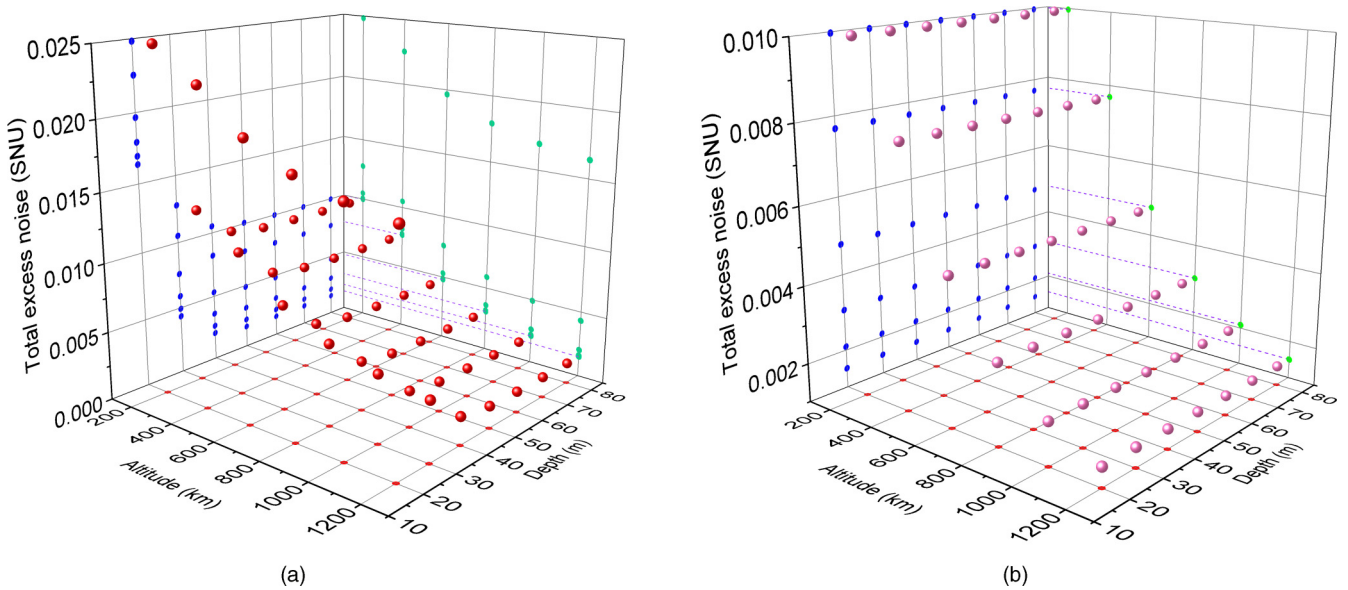

FIG. 10. The worst total excess noise (maximal zenith angle and $\Omega_{\text{fov}} = \pi$) in (a) clear daytime and (b) on a moonless, clear night, respectively. Six cases at different altitudes (from $H = 200$ to 1200 km in steps of 200 km) and seven depths (from $D = 20$ to 80 m in steps of 10 m) are investigated. The dashed lines at the xOz axis plane represent the ENL at their corresponding altitudes.

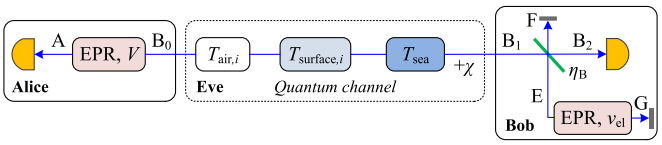

FIG. 11. The equivalent theoretical model of the satellite-to-submarine CV-QKD with Gaussian-modulated states. $T_{\mathrm{air},i}$: atmospheric transmittance; $T_{\mathrm{surface},i}$: transmittance of the fluctuating sea surface; T_{sea}: underwater transmittance at a certain depth; χ: total excess noise; η_{B} and v_{el}: the efficiency and electrical noise of the homodyne detector, respectively.

longer. The minimal excess noise is merely 0.000 46 SNU, and the maximal variance of excess noise is 0.01 SNU.

However, the practical excess noise of the received states may be larger than ENL due to background noise from the atmosphere and seawater. We will discuss the main noise which comes from background light in the air and seawater, which were investigated in Refs. [50,51], respectively. In order to analyze background light noise from the atmosphere, we could image that there is a virtual telescope on the sea surface receiving the signal light and retransmitting the light to the submarine vehicle through the lossy seawater. Therefore, the noise power at the virtual receiver can be expressed as

$$P_{\mathrm{air}} = H_b \times \Omega_{\mathrm{fov}} \times \pi r_0^2 \times B_{\mathrm{filter}}, \tag{20}$$

where H_b is the brightness of the sky background in $\mathrm{W\,m^{-2}\,sr^{-1}\,\mu m^{-1}}$, $\Omega_{\mathrm{fov}} = \pi$ and $r_0 = 1$ m are the field of view and the radius of the virtual telescope, respectively, and B_{filter} is the filter bandwidth. H_b is strongly related to the weather conditions, for example, the typical brightness on a moonless, clear night (1.5×10^{-5} $\mathrm{W\,m^{-2}\,sr^{-1}\,\mu m^{-1}}$) is approximately six orders of magnitude smaller than the value for clear daytime ($1.5\ \mathrm{W\,m^{-2}\,sr^{-1}\,\mu m^{-1}}$) [50]. The field of view relies on the sea surface roughness. For a practical CV-QKD system, most of the background light can be filtered through a homodyne detector that plays the role of a spatial filter [21]. Only photons that are spatially mode matched to the LO produce a significant signal on the detector. Therefore, the value of B_{filter} is mainly determined by the laser used to generate LO. We can take the value of the error range of the laser's output to be 0.01 nm, that is, $B_{\mathrm{filter}} = 0.01$ nm [50]. Figure 9(c) shows the background light noise power from the air based on different brightnesses and fields of view.

Similarly, most of the background light noise in the sea is from the air (the Sun and the sky). Approximately 95% of this light enters the seawater and is absorbed somewhere beneath the surface [51,52]. Therefore, the solar background noise underwater can be obtained by

$$P_{\mathrm{sea}} = L_{\mathrm{sol}} \times \Omega_{\mathrm{fov}} \times \pi r_0^2 \times B_{\mathrm{filter}}, \tag{21}$$

the solar radiance L_{sol} ($\mathrm{W\,m^{-2}\,sr^{-1}\,\mu m^{-1}}$) is given by

$$L_{\mathrm{sol}} = \frac{H_b R L_{\mathrm{fac}} \exp(-cD)}{\pi}, \tag{22}$$

where $R = 1.25\%$ is the underwater reflectance of the downwelling irradiance H_b, $L_{\mathrm{fac}} = 1$ is the factor related to the directional dependence of the underwater radiance, $c = 0.166\ \mathrm{m^{-1}}$ is the attenuation coefficient in clear ocean water, and D is the depth. Figure 9(d) shows the power of underwater background light noise based on different depths and downwelling irradiances. As the depth increases, background noise reduces exponentially. This noise can be ignored when the depth is larger than 50 m.

Given the above, total excess noise can be easily obtained by

$$\epsilon_{\mathrm{total}} = \epsilon_{\mathrm{limit}} + \tau \frac{P_{\mathrm{air}} \exp(-cD) + P_{\mathrm{sea}}}{h\nu}. \tag{23}$$

Note that here h represents Planck's constant (not altitude) and ν is the frequency of the noise photons. τ represents the effective sampling period of the homodyne detector, and it determines how many noise photons are collected during the sampling time. We can apply a homodyne detector with a frequency of 1 GHz and thus $\tau = 1$ ns.

In order to ensure the satellite-to-submarine CV-QKD system has a sufficient level of security, the estimated excess noise should be considered to be in the worst condition (the maximal zenith angle and $\Omega_{\mathrm{fov}} = \pi$). Figure 10 shows the maximal excess noise in clear daytime and on a moonless night. We can see clearly that the excess noise in clear daytime

TABLE I. The parameters to simulate the bit rate of the secret key. All the variances and noises are in SNU.

Variable	Value	Description	References
H	200–800 km	Altitude	
D	20–80 m	Depth	
ζ	0°–76°	Zenith angle	
c	$0.166\ \mathrm{m^{-1}}$	Loss of clean ocean water	[56,57]
r_0	1 m	Receiver radius	[16,33]
V_A	4	Modulated variance	[49]
ϵ_0	0.01	Initial excess noise	[48,49]
β	90%	Reconciliation efficiency	[55]
η_{B}	0.6	Detection efficiency	[55,58]
v_{el}	0.01	Electronic noise of detector	[48]
N	10^{10}	Total photons	[54]
n	$10^{10}/2$	Photons used for key	[54]
f_{ref}	1 MHz	Repetition frequency	
$\bar{\epsilon}$, ϵ_{PE}	10^{-10}	Parameters for privacy amplification	[54]

is higher than the ENL (the dashed lines) when it is at a depth of 20 m. As the depth increases, the total excess noise drops and becomes close to the ENL. For a moonless, clear night, the background noise is not obvious but stays around the ENL.

IV. PERFORMANCE ANALYSIS

The performance of the satellite-to-submarine CV-QKD system will be analyzed in this section. An equivalent theoretical model of the satellite-to-submarine CV-QKD with modulated entangled states is presented in Fig. 11. Alice modulates the initial state with a variance of V_A and measures half of the state (mode A), and the other half (mode B_0) is transmitted through the atmosphere, sea surface, and seawater, in turn. χ represents total excess noise caused by the background light. Bob measures the amplitude or phase quadrature using a homodyne detector which is modeled by placing an EPR input with variance v_{el} and a beam splitter with transmittance η_B before ideal detection.

It is worth noting that the transmittances of the atmosphere and sea surface are not constant but are fluctuating in time. According to previous works [22,23,53], after propagating the fluctuating channel, the overall states degrade into non-Gaussian mixed states after individual channels, thus the Wigner functions of the overall state are the sum of Wigner functions of the states weighted by subchannel probabilities. Eventually, the covariance matrix of the mixed states is governed by two parameters of the attenuation distribution, i.e., the mean value of transmittance and the mean of the square root of transmittance. Therefore, the covariance matrix of the mode AB_1 is expressed by

$$\gamma_{AB_1} = \begin{pmatrix} V\mathbf{I} & T_C\sqrt{V^2-1}\mathbf{Z} \\ T_C\sqrt{V^2-1}\mathbf{Z} & T_B V + 1 - T_B + \chi \end{pmatrix}, \tag{24}$$

with the given notations

$$V = V_A + 1, \quad T_C = \sqrt{T_{\text{sea}}^D}\langle\sqrt{T_{\text{air}}}\rangle\langle\sqrt{T_{\text{surface}}}\rangle,$$
$$T_B = T_{\text{sea}}^D\langle T_{\text{air}}\rangle\langle T_{\text{surface}}\rangle. \tag{25}$$

From the covariance matrix of the state AB_1 it is evident that the total fluctuating channel can be considered as a nonfluctuating channel with transmittance T_C^2 and excess noise caused

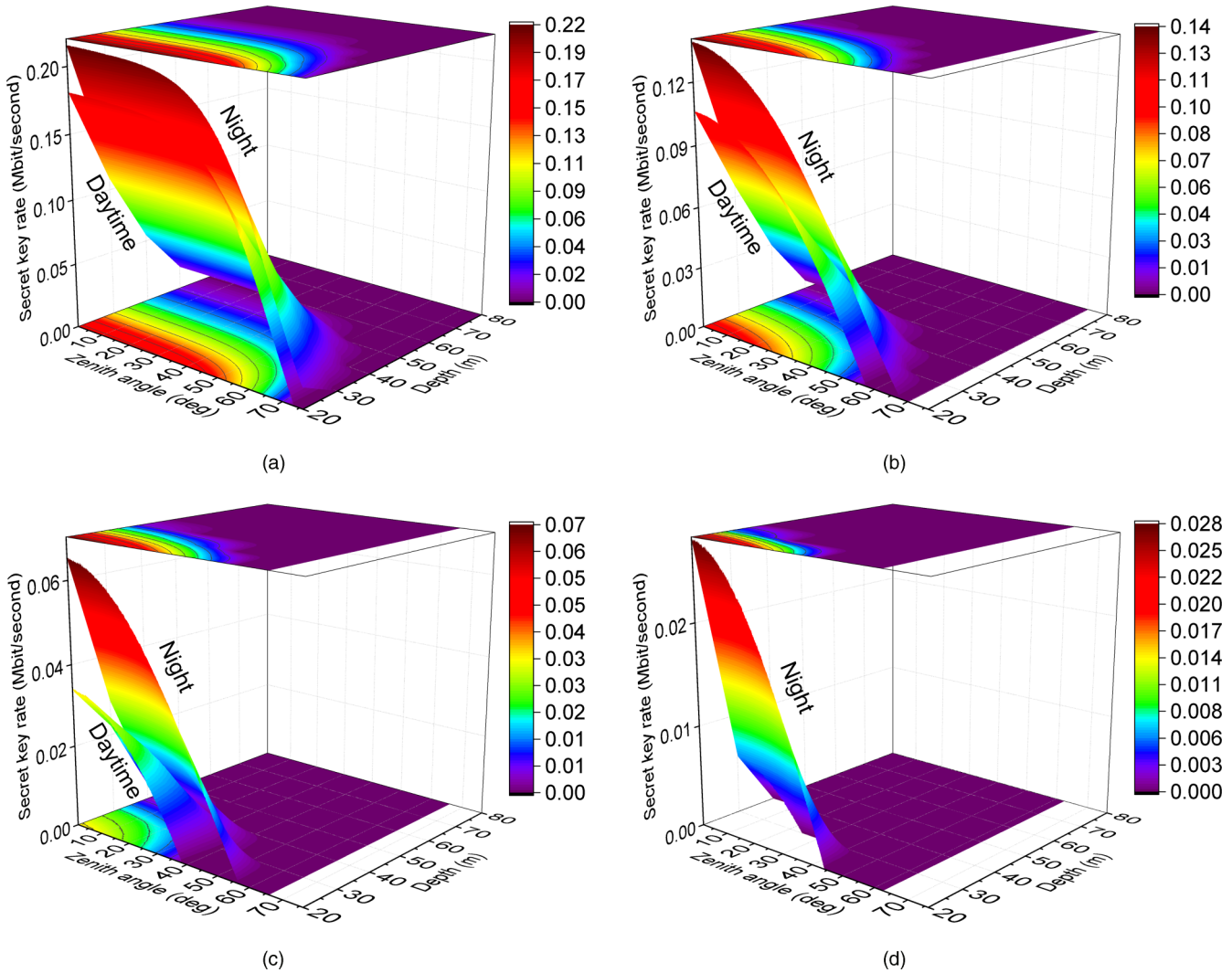

FIG. 12. The secret key bit rate as a function of altitude and depth based on a flat sea surface (i.e., wind speed $v = 0$ m/s and thus $\eta_{\text{deflection}} = 1$). The altitudes of the satellite are set to (a) 200, (b) 400, (c) 600, and (d) 800 km.

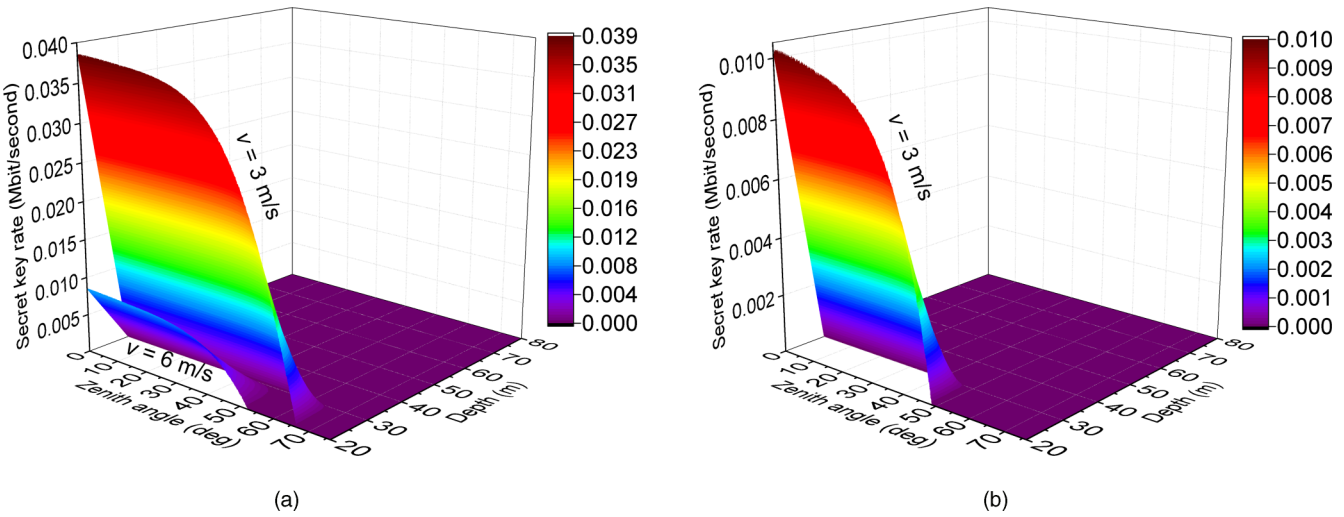

FIG. 13. The bit rate of the secret key (a) in the daytime and (b) at night based on different wind speeds at an altitude of 200 km.

by fluctuations $\xi_f = \mathrm{Var}(T_C)(V-1)$, where $\mathrm{Var}(T_C) = T_B - T_C^2$. The variance of the mode at the submarine becomes $T_C^2(V-1) + \xi_f + \chi + 1$, thus the effect of a fluctuating channel in terms of the covariance matrix could be considered as Gaussian state variance-dependent excess noise [23,53].

The practical security of the CV-QKD system is investigated in Ref. [54], and the secret key rate obtained for a finite-size analysis against a collective attack reads

$$K = \frac{n}{N}\left[\beta I_{\mathrm{AB}} - S_{\mathrm{BE}}^{\epsilon_{\mathrm{PE}}} - \Delta(n)\right], \tag{26}$$

where $\frac{n}{N}$ is the ratio of the number of photons used to establish the secret key to the total number of photons exchanged by Alice and Bob, β is the reconciliation efficiency, the mutual information I_{AB} gives the amount of effective mutual information between Alice and Bob, $S_{\mathrm{BE}}^{\epsilon_{\mathrm{PE}}}$ is defined as the upper bound of the Holevo information compatible with probability ϵ_{PE}, and $\Delta(n)$ is a function corresponding to the privacy amplification. The mutual information I_{AB} using reverse reconciliation can be obtained by

$$I_{\mathrm{AB}} = \frac{1}{2}\log_2\left(\frac{T_B V + 1 - T_B + \chi}{T_B V + 1 - T_B - T_C^2 V + T_C^2/V + \chi}\right), \tag{27}$$

Using the fact that Eve purifies the original states, the value of $S^{\epsilon_{\mathrm{PE}}}$ can also be estimated following Ref. [55]. The last part of Eq. (26), the privacy amplification $\Delta(n)$, reads

$$\Delta(n) = 7\sqrt{\frac{\log_2(2/\bar{\epsilon})}{n}} + \frac{2}{n}\log_2(1/\epsilon_{\mathrm{PA}}), \tag{28}$$

where $\bar{\epsilon}$ and ϵ_{PA} are the smoothing parameter and failure probability of the privacy amplification, respectively.

In order to simulate the secret key rate, we first estimate the mean values $\langle\sqrt{T_{\mathrm{air}}}\rangle$, $\langle\sqrt{T_{\mathrm{surface}}}\rangle$, $\langle T_{\mathrm{air}}\rangle$, and $\langle T_{\mathrm{surface}}\rangle$ by using the Monte Carlo method, which has been already done. Here, 10^6 discrete signals are used to approximate the mean values based on the equations $\langle T_m\rangle = \sum_{i=0}^{10^6} p_{m,i} T_{m,i}$ and $\langle\sqrt{T_m}\rangle = \sum_{i=0}^{10^6} p_{m,i}\sqrt{T_{m,i}}$, where $m = [\mathrm{air},\mathrm{surface}]$. The underwater transmittance at depth of D is calculated by $T_{\mathrm{sea}}^D = \exp[(1 - T_{\mathrm{sea}})D]$. The excess noise is set to its maximum at a certain depth, altitude, and zenith angle in both clear daytime and a moonless, clear night. Using the corresponding parameters in Table I, we investigate the performance of the system in the situations of a flat sea surface and rough sea surface. Figure 12 shows the bit rate of the secret key, $R = f_{\mathrm{rep}}K$, of the satellite-to-submarine CV-QKD system based on the assumption that the sea surface is flat. In other words, the wind speed $v = 0$ m/s and the efficiency of deflection $\eta_{\mathrm{deflection}} = 1$. It is notable that a quantum key can be established successfully even in the daytime at altitudes of 200 and 400 km. Besides, the key rate at night is higher than in the daytime due to their different excess noise. With increasing altitude and depth, the secret key rate sharply decreases and eventually becomes negative. This is because the transmittance of the atmosphere and seawater is increasing. For example, the maximal key rate is 0.22 Mbit/s at an altitude of 200 km at night. However, it is hard to establish keys at an altitude of 800 km in the daytime.

Considering a rough sea surface, the performance of the satellite-to-submarine CV-QKD system will be affected strongly by the wind speed. The transmitted photons will not be received perfectly but deflected out of the receiver aperture. This influence is described by $\eta_{\mathrm{deflection}}$, as discussed above. Figure 13 shows the estimated performance based on different wind speeds at an altitude of 200 km. We can see clearly that the secret key rate decreases sharply with increasing wind speed. Even for a clear, moonless night, the secret key could be established successfully only when the wind speed is 3 or 6 m/s. Therefore, to ensure that the satellite-to-submarine CV-QKD system is operating correctly, Alice and Bob should monitor the weather conditions and choose an appropriate time to share the secret keys.

V. CONCLUSION

We have performed a channel estimation for the CV-QKD system over a satellite-to-submarine link and analyzed its practical performance. First, the channel transmittance which fluctuates randomly in time was estimated using the Monte Carlo method. It could be affected by many factors, including atmospheric turbulence, roughness of the sea surface, wind

speed, zenith angle of the satellite, underwater loss, altitude, etc. On the premise of making a comprehensive consideration of the various effects, the transmittance distributions are obtained using the Monte Carlo approach when the states are transmitting through the atmosphere and sea surface. Second, we estimated the channel excess noise based on the assumption that the noise is mainly caused by background light. Finally, we assessed the system performance at low-Earth orbits in the daytime and at night. The results show that the quantum keys are established successfully over a satellite-to-submarine channel even in the daytime. Most of the parameters in our simulations came from the reported experiments, which made our research strongly practicable in future explorations regarding secure global underwater optical communication networks.

ACKNOWLEDGMENTS

This work was supported by the Fundamental Research Funds for the Central Universities of Central South University and the National Natural Science Foundation of China (Grants No. 61379153 and No. 61572529).

[1] H. M. Oubei, J. R. Duran, B. Janjua, H.-Y. Wang, C.-T. Tsai, Y.-C. Chi, T. K. Ng, H.-C. Kuo, J.-H. He, M.-S. Alouini, G.-R. Lin, and B. S. Ooi, Opt. Express **23**, 23302 (2015).
[2] K. Nakamura, I. Mizukoshi, and M. Hanawa, Opt. Express **23**, 1558 (2015).
[3] C. Shen, Y. Guo, H. M. Oubei, T. K. Ng, G. Liu, K.-H. Park, K.-T. Ho, M.-S. Alouini, and B. S. Ooi, Opt. Express **24**, 25502 (2016).
[4] M. Kong, J. Wang, Y. Chen, T. Ali, R. Sarwar, Y. Qiu, S. Wang, J. Han, and J. Xu, Opt. Express **25**, 21509 (2017).
[5] A. D. Hill, B. Christensen, and P. G. Kwiat, Proc. SPIE **9739**, 973911 (2016).
[6] L. Ji, J. Gao, A.-L. Yang, Z. Feng, X.-F. Lin, Z.-G. Li, and X.-M. Jin, Opt. Express **25**, 19795 (2017).
[7] N. G. Jerlov, *Marine Optics*, Vol. 14 (Elsevier, Amsterdam. 1976).
[8] B. M. Cochenour, L. J. Mullen, and A. E. Laux, IEEE J. Oceanic Eng. **33**, 513 (2008).
[9] P. A. Hiskett and R. A. Lamb, Proc. SPIE **9114**, 91140P (2014).
[10] S. Wang, W. Chen, J.-F. Guo, Z.-Q. Yin, H.-W. Li, Z. Zhou, G.-C. Guo, and Z.-F. Han, Opt. Lett. **37**, 1008 (2012).
[11] C.-Z. Peng, T. Yang, X.-H. Bao, J. Zhang, X.-M. Jin, F.-Y. Feng, B. Yang, J. Yang, J. Yin, Q. Zhang, N. Li, B.-L. Tian, and J.-W. Pan, Phys. Rev. Lett. **94**, 150501 (2005).
[12] P. Villoresi, T. Jennewein, F. Tamburini, M. Aspelmeyer, C. Bonato, R. Ursin, C. Pernechele, V. Luceri, G. Bianco, A. Zeilinger *et al.*, New J. Phys. **10**, 033038 (2008).
[13] S. Wang, Z.-Q. Yin, W. Chen, D.-Y. He, X.-T. Song, H.-W. Li, L.-J. Zhang, Z. Zhou, G.-C. Guo, and Z.-F. Han, Nat. Photonics **9**, 832 (2015).
[14] C. Peuntinger, B. Heim, C. R. Müller, C. Gabriel, C. Marquardt, and G. Leuchs, Phys. Rev. Lett. **113**, 060502 (2014).
[15] H. Zhang, J. Fang, and G. He, Phys. Rev. A **86**, 022338 (2012).
[16] K. Günthner, I. Khan, D. Elser, B. Stiller *et al.*, Optica **4**, 611 (2017).
[17] L.-H. Gong, H.-C. Song, C.-S. He, Y. Liu, and N.-R. Zhou, Phys. Scr. **89**, 035101 (2014).
[18] F. Grosshans and P. Grangier, Phys. Rev. Lett. **88**, 057902 (2002).
[19] F. Grosshans, G. Van Assche, J. Wenger, R. Brouri, N. J. Cerf, and P. Grangier, Nature (London) **421**, 238 (2003).
[20] B. Heim, C. Peuntinger, N. Killoran, I. Khan, C. Wittmann, C. Marquardt, and G. Leuchs, New J. Phys. **16**, 113018 (2014).
[21] D. Elser, T. Bartley, B. Heim, C. Wittmann, D. Sych, and G. Leuchs, New J. Phys. **11**, 045014 (2009).
[22] Y. Guo, C. Xie, Q. Liao, W. Zhao, G. Zeng, and D. Huang, Phys. Rev. A **96**, 022320 (2017).
[23] V. C. Usenko, B. Heim, C. Peuntinger, C. Wittmann, C. Marquardt, G. Leuchs, and R. Filip, New J. Phys. **14**, 093048 (2012).
[24] D. Vasylyev, A. A. Semenov, and W. Vogel, Phys. Rev. Lett. **117**, 090501 (2016).
[25] C. Cox and W. Munk, J. Opt. Soc. Am. **44**, 838 (1954).
[26] M. Hieronymi, Opt. Express **24**, A1045 (2016).
[27] D. Huang, P. Huang, D. Lin, C. Wang, and G. Zeng, Opt. Lett. **40**, 3695 (2015).
[28] B. Qi, P. Lougovski, R. Pooser, W. Grice, and M. Bobrek, Phys. Rev. X **5**, 041009 (2015).
[29] D. B. S. Soh, C. Brif, P. J. Coles, N. Lütkenhaus, R. M. Camacho, J. Urayama, and M. Sarovar, Phys. Rev. X **5**, 041010 (2015).
[30] X. Jin, J. Ren, B. Yang *et al.*, Nat. Photonics **4**, 376 (2010).
[31] B. Wozniak and J. Dera, *Light Absorption in Sea Water*, Vol. 33 (Springer, Berlin, 2007).
[32] C. D. Mobley, *Light and Water: Radiative Transfer in Natural Waters* (Academic, New York, 1994).
[33] C. Bonato, A. Tomaello, V. D. Deppo, G. Naletto, and P. Villoresi, New J. Phys. **11**, 045017 (2009).
[34] L. C. Andrews, R. L. Phillips, and C. Y. Young, Opt. Eng. **39**, 39 (2000).
[35] F. Dios, J. A. Rubio, A. Rodríguez, and A. Comerón, Appl. Opt. **43**, 3866 (2004).
[36] L. C. Andrews and R. L. Phillips, *Laser Beam Propagation through Random Media*, Vol. 152 (SPIE, Bellingham, WA, 2005).
[37] R. R. Beland, *Propagation through Atmospheric Optical Turbulence*, Vol. 2 (SPIE, Bellingham, WA, 1993), pp. 157–232.
[38] C. Qing, X. Wu, X. Li, W. Zhu, C. Qiao, R. Rao, and H. Mei, Opt. Express **24**, 13303 (2016).
[39] D. P. Dee, S. M. Uppala, A. J. Simmons, P. Berrisford *et al.*, Q. J. R. Meteorol. Soc. **137**, 553 (2011).
[40] R. J. Glauber, Phys. Rev. **131**, 2766 (1963).
[41] D. Y. Vasylyev, A. A. Semenov, and W. Vogel, Phys. Rev. Lett. **108**, 220501 (2012).
[42] D. Vasylyev, A. A. Semenov, W. Vogel, K. Günthner, A. Thurn, O. Bayraktar, and C. Marquardt, Phys. Rev. A **96**, 043856 (2017).
[43] E. B. Kraus and J. A. Businger, *Atmosphere-Ocean Interaction*, Vol. 27 (Oxford University Press, Oxford, U.K., 1994).
[44] A. Borovoi, A. Konoshonkin, and L. Kolokolova, J. Quant. Spectrosc. Radiat. Transfer **113**, 2542 (2012).
[45] M. Chami, B. Lafrance, B. Fougnie, J. Chowdhary, T. Harmel, and F. Waquet, Opt. Express **23**, 27829 (2015).
[46] V. Ross, D. Dion, and G. Potvin, J. Opt. Soc. Am. A **22**, 2442 (2005).

[47] G. L. Clarke and H. R. James, J. Opt. Soc. Am. **29**, 43 (1939).
[48] B. Qi, W. Zhu, L. Qian, and H.-K. Lo, New J. Phys. **12**, 103042 (2010).
[49] D. Huang, P. Huang, D. Lin, and G. Zeng, Sci. Rep. **6**, 19201 (2016).
[50] E. Miao, Z. Han, S. Gong, T. Zhang, D. Diao, and G. Guo, New J. Phys. **7**, 215 (2005).
[51] S. Jaruwatanadilok, IEEE J. Sel. Areas Commun. **26**, 1620 (2008).
[52] J. W. Giles and I. N. Bankman, in *MILCOM 2005-2005 IEEE Military Communications Conference*, Vol. 3 (IEEE, New York, 2005), pp. 1700–1705.
[53] R. Dong, M. Lassen, J. Heersink, C. Marquardt, R. Filip, G. Leuchs, and U. L. Andersen, Phys. Rev. A **82**, 012312 (2010).
[54] A. Leverrier, F. Grosshans, and P. Grangier, Phys. Rev. A **81**, 062343 (2010).
[55] S. Fossier, E. Diamanti, T. Debuisschert, R. Tualle-Brouri, and P. Grangier, J. Phys. B **42**, 114014 (2009).
[56] J. Xu, Y. Song, X. Yu, A. Lin, M. Kong, J. Han, and N. Deng, Opt. Express **24**, 8097 (2016).
[57] L. Prieur and S. Sathyendranath, Limnol. Oceanogr. **26**, 671 (1981).
[58] J. Lodewyck, M. Bloch, R. García-Patrón, S. Fossier *et al.*, Phys. Rev. A **76**, 042305 (2007).